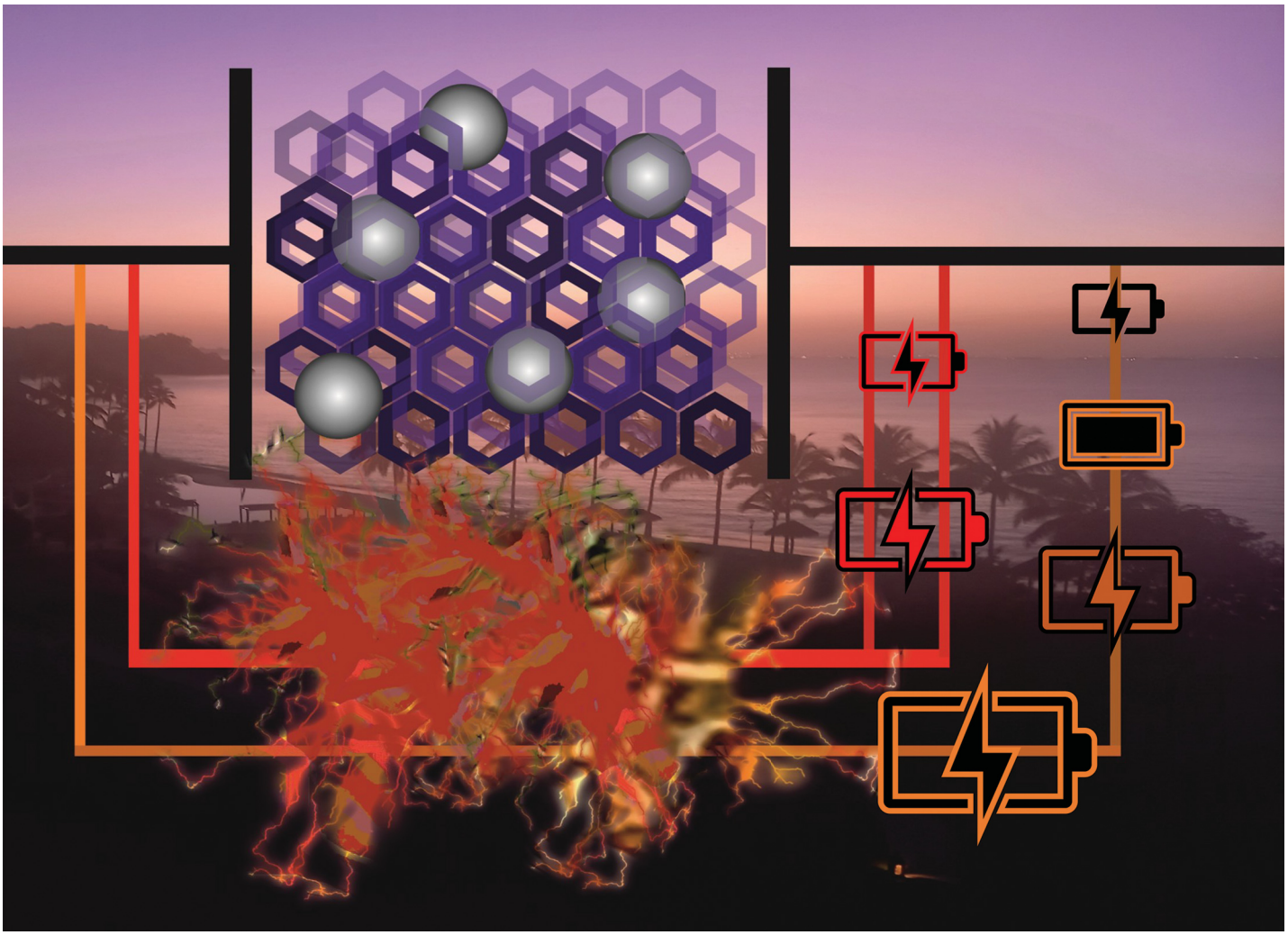

Showcasing research from Professor Plonska-Brzezinska's laboratory, Department of Organic Chemistry, Medical University of Bialystok, Poland.

Rational design of carbon nanocomposites with hierarchical porosity: a strategy to improve capacitive energy storage performance

The covalent triazine frameworks (CTFs) were organized three-dimensionally on the carbon nano-onion (CNO) surface, creating CTF–CNO systems with organized hierarchical porosity. High porosity, about 2000 $m^2 g^{-1}$, the presence of interconnected pores and highly graphitized domains, and a high percentage of the pyridinic-N, the pyrrolic-N, and graphitic-N atoms significantly increased the electrochemical performance of the obtained composites. The efficient combination of all these factors made composites excellent electrode materials. Due to these features, the CTF–CNO materials showed attractive properties for practical applications in electrochemistry.

As featured in:

See Agnieszka Hryniewicka, Marta E. Plonska-Brzezinska *et al.*, *Mater. Adv.*, 2024, **5**, 1065.

ROYAL SOCIETY OF CHEMISTRY

rsc.li/materials-advances

Registered charity number: 207890

Materials Advances

ROYAL SOCIETY OF CHEMISTRY

PAPER

View Article Online
View Journal | View Issue

Cite this: *Mater. Adv.*, 2024, 5, 1065

Rational design of carbon nanocomposites with hierarchical porosity: a strategy to improve capacitive energy storage performance†

Agnieszka Hryniewicka, *[a] Joanna Breczko,[ab] Gabriela Siemiaszko, [a] Krzysztof Brzezinski, [c] Anna Ilnicka, [d] Artur P. Terzyk[d] and Marta E. Plonska-Brzezinska *[a]

Received 14th November 2023,
Accepted 16th November 2023

DOI: 10.1039/d3ma01003a

rsc.li/materials-advances

Covalent triazine frameworks (CTFs) constitute an emerging class of high-performance materials due to their porosity and the possibility of structural control at the molecular or atomic level. However, use of CTFs as electrodes in supercapacitors is hampered by their low electrical conductivity and a strong stacking effect between adjacent CTF sheets. Herein, two series of hybrid carbon nano-onion-based CTFs are designed and successfully synthesized using an ionothermal process at 700 °C. The CTFs could undergo framework growth in two or four directions, which was related to a defined number of nitrile groups in the substrate. CTF counterparts without carbon nano-onions were also synthesized as reference materials. The carbon nanocomposites exhibited excellent specific capacitances, with the highest value exceeding 495 F g^{-1}. It should be emphasized that the specific capacitance value of hybrid materials was 1.5–2 times higher than that of the reference CTFs. This study examined the factors responsible for such a significant increase in electrochemical efficiency. This strategy has significantly expanded the scope and application of CTFs as electrode materials for electrochemical energy storage systems.

1. Introduction

The demand for advanced materials used for power devices is constantly growing, and the focus is on the search for safer and more efficient solutions. These include, among others, capacitors that are counted to future technology and devices with unique electrochemical properties that can store a large amount of electric charges. In most cases, the maximum charge is related to the electrode surface area, accessibility to electrolyte ions, surface morphology, and electrical conductivity.[1] According to energy storage mechanisms, capacitors can be classified as electric double-layer capacitors (EDLCs) and pseudocapacitors.[2] EDLCs are superior to conventional batteries due to their valuable properties, such as high power density, long durability, and fast charging–discharging.[3] The search for improving EDLC performance is directly connected to the development of novel materials for electrodes, which will ensure the appropriate operational parameters of the devices. So far, carbon materials focusing on nano-structured and nano-engineered forms have been commonly used in energy storage devices, including supercapacitors (SCs).[1,2,4] A sizeable active surface area and high porosity should primarily characterize the electrode material made of nanoscale materials—theoretically, the higher the surface area and electrolyte concentration, the higher the capacitance values.

In connection with the above guidelines, we proposed a combination of carbon nanostructures and spherical multilayer fullerenes (called carbon nano-onions, CNOs) with covalent triazine frameworks (CTFs) to create nanocomposites for SCs.[5,6] The combination of materials with differential chemical characters increases the capacity and porosity of electrodes, reaching better electrochemical performances.[7] Moreover, combining faradaic and non-faradaic processes in SCs can achieve higher energy and power density while maintaining long-term electrochemical stability. Our studies show that using CNOs during the synthesis of macromolecular systems may organize

[a] *Department of Organic Chemistry, Faculty of Pharmacy with the Division of Laboratory Medicine, Medical University of Bialystok, Mickiewicza 2A, 15-222 Bialystok, Poland. E-mail: agnieszka.hryniewicka@umb.edu.pl, marta.plonska-brzezinska@umb.edu.pl*
[b] *Faculty of Chemistry, University of Bialystok, Ciolkowskiego 1K, 15-245 Bialystok, Poland*
[c] *Department of Structural Biology of Prokaryotic Organisms, Institute of Bioorganic Chemistry, Polish Academy of Sciences, Noskowskiego 12/14, 61-074 Poznan, Poland*
[d] *Faculty of Chemistry, Nicolaus Copernicus University in Torun, Gagarin Street 7, 87-100 Torun, Poland*

† Electronic supplementary information (ESI) available. See DOI: https://doi.org/10.1039/d3ma01003a

the organic framework of oligomers,[8] polymers[9,10] or CTFs[5] and alter the uniform distribution of pores and pore sizes (micropores (<2 nm), mesopores (2–50 nm) and macropores (>50 nm)) within the materials. Additionally, the combination of two components also guarantees an increase in the total porosity of the material, which is critical when using them as electrodes in SCs.

We are using CNOs obtained *via* thermal annealing of nanodiamonds, which leads to the formation of nanostructures of small sizes (diameter in the range of 5–6 nm).[11] The CNO is a zero-dimensional carbon nanoparticle with a multilayer spherical graphite structure of 1.4–50 nm in diameter.[11] The large graphite surface of CNOs (with sp^2-hybridized C atoms) enables the formation of supramolecular systems using covalent[12–14] and non-covalent functionalization, for example, through electrostatic, van der Waals, and π–π interactions.[15,16] These functionalizations allow controlling of the physical and chemical properties of carbon nanostructures, which in turn enable their versatile applications.[1,14,17–21]

We used nitrogen-rich triazine units that form CTFs to modify the CNO surface.[5,6] CTFs are stable and can withstand harsh acidic or alkaline conditions that are destructive to other porous organic polymers. CTFs possess highly conjugated structures and exhibit semiconductive properties, making it possible to use them in SCs. Notably, the high N atom content and the large surface area must be considered to achieve high efficiency in energy storage devices.[22] The first reports of the application of CTFs as SCs date back to 2012.[23–25] There have been few reports of CTFs with specific capacitance values exceeding 500 F g^{-1}, *i.e.*, anthracene-based CTFs,[26] a series of bicarbazole-based CTFs,[27] pyrene-functionalized CTFs,[28] and polyethynylbenzonitrile-derived frameworks.[29] Other CTFs with relatively high capacitance include tetracyanoquinodimethane,[30] bipyridine,[31] halogen-substituted derivatives,[32] and pyridine.[33] These materials have suitable N atom contents, hierarchical micro-mesoporous properties, and high specific surface areas with abundant channels for charges, resulting in remarkable cycle stability, high capacity retention, and excellent coulombic efficiencies.

Herein, we design CTFs with different pore diameters and their hybrids with CNOs. Symmetrically substituted moieties with nitrile groups were used to obtain the desired CTFs. One of them, *i.e.*, tetraarylpyrrole[3,2-*b*]pyrrole, was applied for the first time by our group as a core in a CTF structure.[6] It is well known that a small amount of the CNO is enough to markedly increase the surface area of the hybrid material and improve its electrochemical properties.[34]

2. Results and discussion

2.1. Syntheses of CTF and CTF–CNO materials

Four compounds were selected for syntheses of pristine CTFs and CNO-based CTFs. Two of them, namely 1,4-dicyanobenzene (**2CN-1**)[23,35] and 7,7,8,8-tetracyanoquinodimethane (**4CN-1**),[30] are known as building blocks of organic skeletons, forming two-dimensional (2D) macrostructures with a repeating structural organization (Fig. 1). We used known substrates to study the effects of CNO additives on the structural and chemical properties of the synthesized materials. The other two monomers are pyrrolopyrroles, such as 1,4-bis(6-methylbenzo[*d*]thiazol-2-yl)-2,5-bis(4-cyanophenyl)-1,4-dihydropyrrolo[3,2-*b*]pyrrole (**2CN-2**) and 1,2,4,5-tetrakis(4-cyanophenyl)-1,4-dihydropyrrolo[3,2-*b*]pyrrole (**4CN-2**), which have never been used for these purposes. The new monomers differed in the number of benzonitrile groups substituted in the pyrrolopyrrole core. **2CN-2** and **4CN-2** contained two and four benzonitrile substituents, respectively. Additionally, in the **2CN-2** structure, two benzothiazole substituents are linked to the pyrrolepyrrole core. These substrates synthesized CTFs covalently attached to the CNO surface (**CTF–CNO**).

Given the experimental determination of the structure, it was expected that tetraaryl-substituted 1,4-dihydropyrrolo[3,2-*b*]pyrrole monomers with four –CN groups would form a more cross-linked, less ordered framework.[36] Conversely, such a skeleton should have a higher N atom content. Adding relatively large CNO structures can result in the framework organization in the three-dimensional (3D) architecture, where the CNO may separate the adjacent CTF sheets. It is very desirable in the case of amorphous frameworks composed of substrates with four –CN groups. Moreover, the nanostructural carbon size may induce a specific orientation of the framework in space.

Pyrrolepyrroles were synthesized in a condensation reaction using iron(III) perchloride hydrate as a catalyst using a simple, straightforward methodology.[37] Pyrrolopyrrole-based and commercially available substrates were pyrolyzed at 700 °C with $ZnCl_2$ in an ionothermal process to obtain pristine CTFs (Fig. 1). The covalently modified CNOs (**CNO-CN**, 5 wt%)[34] were pyrolyzed with the appropriate monomers to obtain the hybrid **CTF–CNO** materials. $ZnCl_2$ can act as a catalyst, solvent, and porogen.

2.2. Structural characterization of CTF and CTF–CNO

Fourier transform infrared (FTIR) spectroscopy was used to evaluate the synthesis of **CTF** and **CTF–CNO**. The trimerization of all the substrates was confirmed by FTIR spectroscopy (Fig. 2). The complete trimerization of the monomers was indicated by the absence of a carbonitrile band at 2230 cm^{-1} in the spectra of the formed materials (Fig. 2A–C, respectively).[35] Furthermore, all CTFs gave rise to a band at approximately 1630 cm^{-1}, the characteristic of the C=N stretching vibration, indicating the successful formation of triazine graphitic-like domains (Fig. 2B and C).[38] This band may also be attributed to aromatic C=C skeletal vibrations, indicating the presence of a graphite structure.[39] Moreover, the bands between 1550 and 1120 cm^{-1} correspond to the N-doped graphitic domains, which are related to graphitic C=C vibrations, N=H stretching, C–N stretching of aromatic amines in benzenoid units, and in-plane distortion vibrations of the C–H bonds in benzene rings.[39–41] The broad overlapping bands in the range of 2900–2800 cm^{-1} were attributed to stretching deformation vibrations of aromatic C–H, suggesting the presence of sp^3-hybridized carbon atoms in the

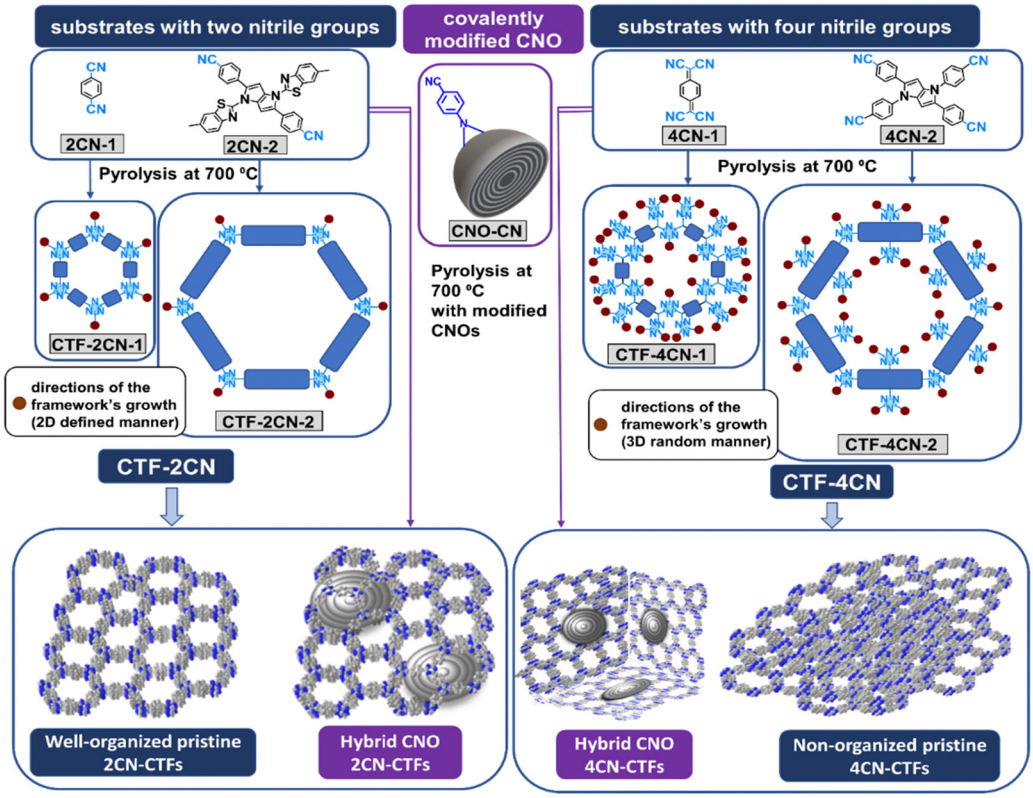

Fig. 1 Representative schematic synthesis of **CTF** and **CTF–CNO** materials.

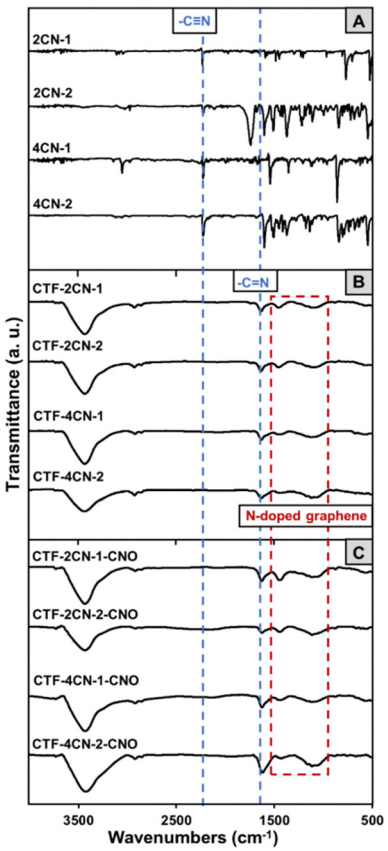

Fig. 2 FTIR spectra of (A) monomers, (B) **CTF** materials and (C) **CTF–CNO** materials.

CTF and **CTF–CNO** materials (Fig. 2B and C).[42] Moreover, a broad, strong band extending from 3600 to 3000 cm^{-1} was attributed to the stretching vibrations of N–H and aromatic (=C–H) groups and their intra- and intermolecular hydrogen bonding (Fig. 2B and C).

The solid-state ^{13}C NMR measurement further confirmed the structures of **CTF** and **CTF–CNO** materials. As shown in Fig. S6 (ESI†), aromatic regions are located in the range of 140 to 110 ppm in all spectra of CTFs. Moreover, the chemical shifts at 165–170 ppm are present that can be assigned to the carbon signal from triazine rings.[43] Although the relative intensity of this peak is small, its presence indicated the formation of triazine rings. The signal constituting the aromatic region becomes broader for **CTF–CNO** hybrids (**CTF-2CN-1-CNO** and **CTF-4CN-1-CNO**), which may indicate a higher degree of carbonization.[44] In the spectra of pyrrolo[3,2-*b*]pyrrole-based CTFs (pristine and hybrids of **CTF-2CN-2** and **CTF-4CN-2**), there are more aromatic carbon signals, which is related to the presence of pyrrole carbons (see the spectrum of the substrate **2CN-2**, Fig. S2, ESI†).

X-ray photoelectron spectroscopy (XPS) was used to determine the elemental compositions of the **CTF** and **CTF–CNO** materials. The results indicated that all the studied materials contain C and N atoms with contents between 82 and 91 at% and 4 and 9.5 at%, respectively (Table S1, ESI†). The distribution of elements was defined due to the deconvolution of the high-resolution spectral C 1s (Fig. S5, ESI†) and N 1s (Fig. 3) regions. The C 1s XPS analysis showed that all the materials

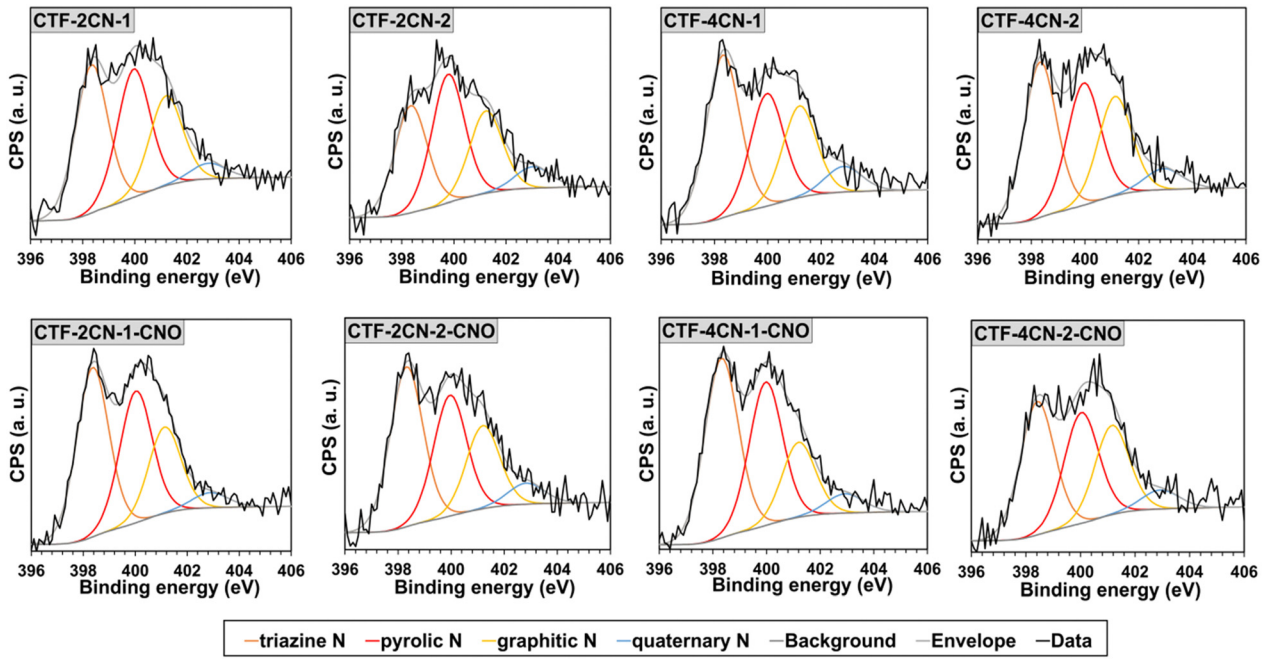

Fig. 3 XPS N 1s spectra of the **CTF** and **CTF–CNO** spectral regions.

had a similar distribution pattern of functional groups and defects (Fig. S5 and Tables S2, S3, ESI†). The prominent peak at ~284.5 eV was assigned to the sp^2-hybridized C atom in C=C (graphitic/aromatic structure).[39,45,46] The peaks at ~285.0, ~285.6, and ~286.4 eV were related to the C–H sp^3, C–C sp^3, and C=N moieties, respectively (Tables S2 and S3, ESI†).[46] There were also peaks attributed to C–O–C, C=O, and C–N–C groups, with a total content below 10 at%.[45,46] It should be noted that **CTF-2CN-2** triazine has a significant content of C–N–C groups in its structure (~288.9 eV),[46] compared to other triazines, corresponding to approximately 5 at%.

All the materials also containing some defects (~283.8 eV), which in the CTF, were mainly related to the presence of single and double C vacancies.[47,48] After the covalent immobilization of the CTF sheets on the CNO surface, the number of defects in the materials increased, which was mainly attributed to the disruption of the C=C bonds with sp^2-hybridization in the CNO.

An increase in sp^2-hybridized C atoms and a decrease in sp^3-hybridized C atoms for the pair of **CTF-2CN-2-CNO** and **CTF-2CN-2** and a couple of **CTF-4CN-2-CNO** and **CTF-4CN-2** (Tables S2 and S3, ESI†), respectively, displayed improvement in graphitic-like domains in the systems. The opposite transformation of C atoms was observed for **CTF-2CN-1** after CNO addition (**CTF-2CN-1-CNO**). Moreover, the elemental compositions of CTF materials were analyzed by elemental analysis, and the results are summarized in Table S1 (ESI†), along with the distribution of elements obtained from XPS. The number of N atoms expressed as a percentage determined by elemental analysis and XPS is almost always consistent. By elemental analysis, we also confirmed the presence of sulfur atoms for **CTF-2CN-2** and **CTF-2CN-2-CNO** at 9.23 and 11.36%, respectively. We observed some discrepancies in the amount of determined carbon. These differences may result from the nature of the measurements of both methods and their accuracy. XPS is the surface analysis of materials. The elemental analysis leads to the complete degradation of the materials and determines the content of individual elements in the entire volume.

The deconvoluted XPS spectra for the N 1s binding state indicated that N was present in four different chemical environments in the **CTF** and **CTF–CNO** materials (Fig. 3 and Tables S4, S5, ESI†). Three peaks, namely, pyridinic-N in the covalent triazine skeleton (~398.3 eV),[49,50] pyrrolic-N (~400.0 eV),[51] and tertiary amine in a graphitic network (graphitic-N, ~401.2 eV), were dominant in the spectra of all the synthesized materials.[51,52] The pyridinic-N atoms were the main contribution, with a content of approximately 40 at% for all the materials, excluding **CTF-2CN-2**, for which this value was approximately 31 at%, followed by pyrrolic-N (about 28–34 at%) and graphitic-N (about 21–25 at%) (Tables S2–S5, ESI†). The graphitic-N atoms were originated from sp^2-hybridized N, bonded with three adjacent sp^2-hybridized C atoms.[53] The N atoms were partially bound in the hexagonal network of graphene. The N atoms appearing in a much smaller amount from 4.1 to 7.1 at% were assigned to the quaternary graphitic N atoms (~402.8 eV).[50,52]

High-resolution transmission electron microscopy (HRTEM) studies were performed to analyze the structural organization of the CTF, as well as the effect of adding CNOs to the 2D triazine frameworks. Amorphous phases and crystalline zones were present in all the synthesized materials.[54] This heterogeneity in structure may result in higher structural stability and higher conductivity of the hybrid materials. Moreover, the HRTEM images of **CTF–CNO** hybrids showed the presence of

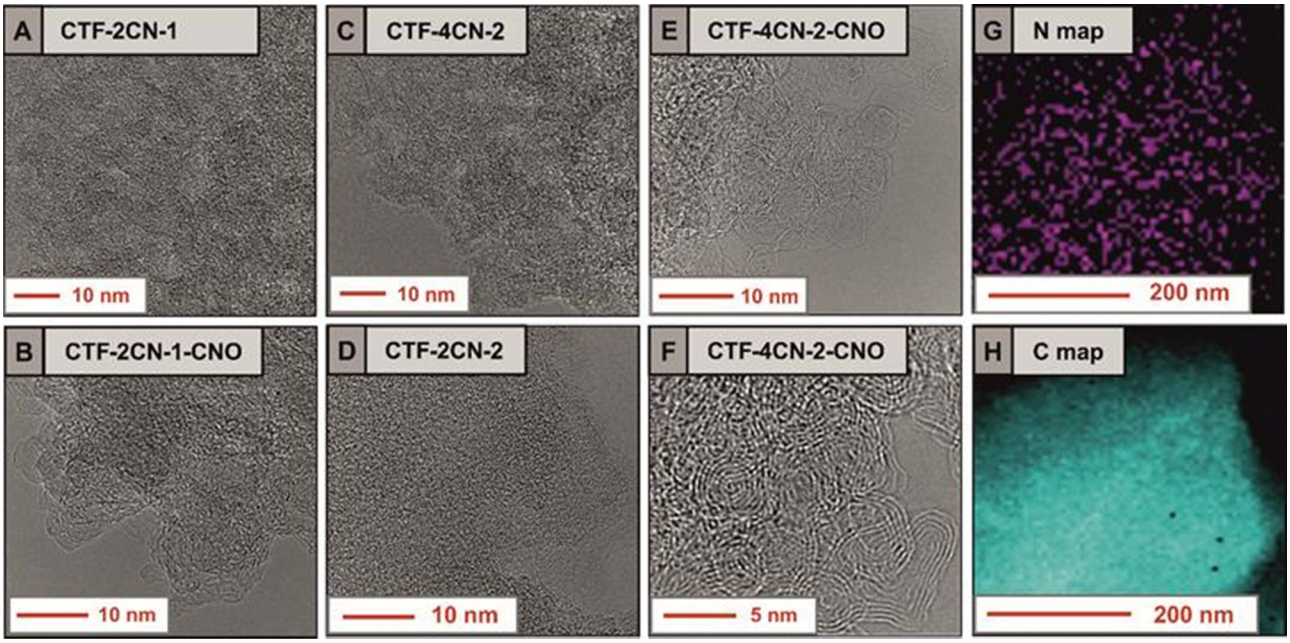

Fig. 4 Fig. 4 (A)–(F) HRTEM images of the **CTF** and **CTF–CNO** materials; STEM EDS maps of the elemental distribution in **CTF-4CN-2-CNO** of (G) N atoms and (H) C atoms.

CNOs and graphene ribbons in the structure (Fig. 4F), which increased the crystallinity of the materials. Scanning transmission electron microscopy (STEM) in conjunction with energy-dispersive X-ray (EDX) spectroscopy was used to evaluate the distribution of atoms constituting the synthesized materials and their elemental homogeneity (Fig. 4G and H). The STEM-EDX maps recorded after scanning the **CTF-4CN-2-CNO** surface show the distribution of the C and N atoms in the material, with a significant predominance of C. The N atoms were not evenly distributed in the material.

Fig. 4G clearly shows areas with a large amount of N (marked in purple) and darkened areas, which indicate the lack of N. The violet regions, indicating the presence of N atoms, replicated the skeleton of the CTF; therefore, the shaded areas correspond to pores present in the material, which were interconnected. The material's structure with interconnected pores is expected to favor the transport of ions to the electrode surface, which should effectively affect the electrochemical properties of the material.[55] In short, in the case of electrodes with many interconnected pores, an even distribution of contact between the electrode and the electrolyte is ensured,[56] improving the mass transfer of electrolyte ions into the electrode.[55,57] At the same time, in the case of materials with high graphitization and porosity, during repeated charging and discharging of the electrodes, they maintain a 3D structure very well, which ensures their high mechanical stability. Thus, a further advantage of such electrodes is that their porous construction allows the interconnected walls to expand into the open pores, preventing the walls from pulverizing while exhibiting an extremely high level of structural integrity.[57,58]

Our X-ray powder diffraction (XRD) experiments indicated the transformation of nanodiamond (ND) particles into CNOs at 1650 °C (Fig. 5), at which point we synthesized CNOs. The XRD patterns of the ND and CNO show the presence of a mixture of various phases with different intensities for both materials. For the ND, the most substantial reflection at approximately $2\theta = 43.8^\circ$ corresponded to the diffraction on the (111) basal plane of the diamond structure.[59] A broad peak in the 20–27° range was also observed, suggesting a certain amount of a graphite-like phase.[60,61] For the CNO nanostructures, these two reflections were also present in similar degrees of theta angles, but their intensity and nature differed. An asymmetric second peak with a maximum of approximately 43.0° was observed, which was attributed to the (002) and (100) graphite planes.[62] The broad asymmetric peak centered at approximately 23–27° suggests contributions of some sp^2-bonded carbons in the CNO structures. Its asymmetry can be divided into two subpeaks characteristic of turbostratic and graphitic carbon.[63,64] For all **CTF** and **CTF–CNO** materials, these relatively broad peaks attributed to sp^2- and sp^3-hybridized C atoms were also predominant. Diffraction broadening originates primarily from the size of the grains. However, a further influence of strains and defects in the semi-crystal material on diffraction broadening cannot be excluded and requires additional studies.

Some other reflections, which were sharp with low intensity, were observed for **CTF-2CN-1-CNO** and **CTF-4CN-2-CNO**. The peaks at 27.6° and 28.9° were attributed to a layered structural motif, stacked chains of *s*-triazine and tri-*s*-triazine units,[65–67] which can be attributed to a pseudo-(002) stacking motif of the graphitic carbon nitride (g-C_3N_4) domains, similar to the turbostratic phase of graphite.[68] The interlayer stacking reflection is the characteristic of conjugated aromatic structures – polymerized triazine- and tri-*s*-triazine-based g-C_3N_4.[69,70] This arrangement is so-called triazine-based g-C_3N_4.[69,71] These motifs

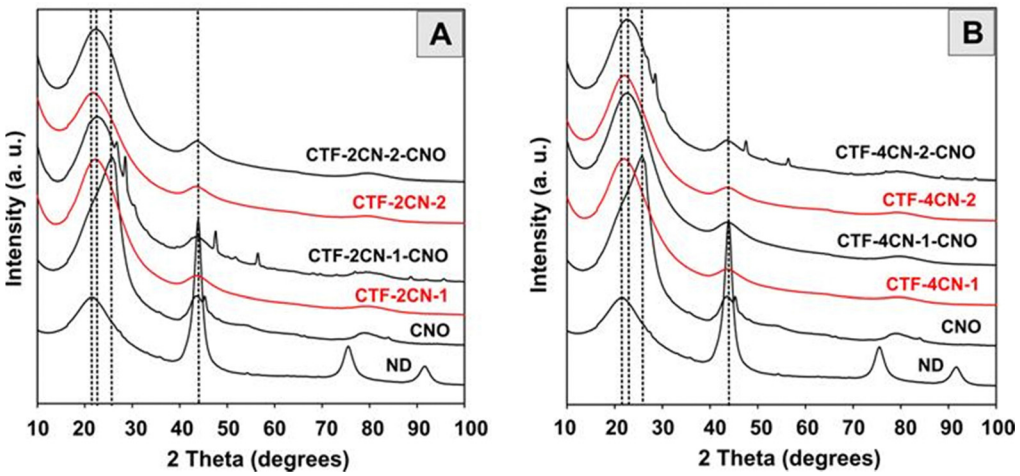

Fig. 5 XRD studies of (A) and (B) NDs and CNOs; (A) **CTF-2CN-1**, **CTF-2CN-1-CNO**, **CTF-2CN-2**, and **CTF-2CN-2-CNO**; and (B) **CTF-4CN-1**, **CTF-4CN-1-CNO**, **CTF-4CN-2** and **CTF-4CN-2-CNO**.

can be formed under several conditions, including the appropriate number of N atoms relative to the number of C atoms, the pyrolysis temperature, the pore structure, the planarity of the triazine ring, *etc.* The other two signals for **CTF-2CN-1-CNO** and **CTF-4CN-2-CNO** were the observable characteristics of the graphitic structure. These results reveal the (101) and (004) reflections at 47.4° and 56.29° (**CTF-2CN-1-CNO**) and 56.09° (**CTF-4CN-2-CNO**) and the characteristic of g-C_3N_4.[72] These microstructures suggest the presence of highly graphitized domains in the materials.

The **CTF** and **CTF–CNO** materials decompose almost totally in an air atmosphere, showing one significant weight loss between 430 and 700 °C with the maximum degradation at 540–610 °C (Fig. S10, ESI†). The second, much smaller degradation of up to 10% of the materials occurs up to 250 °C, with a maximum at about 140 °C. The more significant weight loss is observed for nanocomposites containing **CTF-4CN-1** and **CTF-4CN-2**, *e.g.*, systems containing more heterocyclic rings in the skeleton. It should be emphasized that this stage is observed in both pristine **CTFs** and nanocomposites and has an analogous course. This proves that the **CTF** and CNO after the pyrolysis process at high temperatures indicate a high chemical and structural similarity of the obtained carbonaceous materials; the **CTF** is subject to the graphitization process. Both the CTF and the CNO are made of pentagonal and hexagonal carbon rings. Generally, pyrolyzed materials show high thermal stability up to 600 °C, and their decomposition profiles are similar, degrading continuously over the entire temperature range applied. The **CTF** and **CTF–CNO** materials pyrolyzed at high temperatures have a high degree of structural organization and graphitization, resulting in increased thermal stability.

2.3. Textural and electrochemical characteristics of CTF and CTF–CNO

Low-temperature nitrogen adsorption–desorption isotherms were measured at −196 °C. Using Brunauer–Emmett–Teller (BET) theory, the surface area (S_{BET}) was calculated *via* the approach proposed by Rouquerol *et al.*[73] The pore size distribution (PSD) was calculated by nonlocal density functional theory (DFT) for slit-like carbon nanopores.[74–76] Considering the mechanism of these processes, the differential PSDs were analyzed (Fig. 6 and Fig. S7, ESI†), and cumulative nanopore volume distributions (Fig. S7, ESI†) and the micropore (V_{micro}) and mesopore (V_{meso}) values were calculated (Table 1).

Most of the nitrogen adsorption–desorption curves shown in Fig. 6 (**CTF-2CN-1**, **CTF-2CN-2**, and **CTF-4CN-2**) are type IVa isotherms according to the IUPAC classification and the characteristic of materials with a predominance of mesopores. The exception is the type I isotherm recorded for **CTF-4CN-1** (Fig. 6C), which suggests the microporous nature of this sample. The addition of CNOs impacted the **CTF** material porosity, and the observed effect strongly depended on the synthesized systems' structural geometry. Namely, the diameter of the CTF ring (see Fig. 1) determined the total pore volume, including the share of micro- and mesopores and S_{BET} (see Table 1). There is an ongoing debate over applying the BET evaluation to evaluate the specific surface area of materials with a relevant proportion of micropores and small mesopores.[77,78] Despite these doubts, we decided to use this model because it allows us to compare our results with the literature data (Table S6, ESI†), and the obtained surface area is in fact apparent. In the case of **CTF-2CN-1-CNO** and **CTF-4CN-1-CNO** materials containing smaller CTF rings in their structures (Fig. 1), the introduction of CNOs increased S_{BET} (Table 1).

In contrast, the **CTF-2CN-2-CNO** and **CTF-4CN-2-CNO** materials, with a larger diameter of the CTF rings, exhibited lower S_{BET} values than the corresponding CTFs without CNOs (Fig. 1 and Table 1). In addition, it should be emphasized that the increase in porosity observed for the **CTF-2CN-1-CNO** and **CTF-4CN-1-CNO** systems originated *via* a different mechanism because of the diverse nature of the pristine CTF, namely, the nanoporosity (micro- and mesoporosity with pores having diameters smaller than *ca.* 100 nm). For the **CTF-2CN-1-CNO** system, the appearance of CNOs led to a reduction in the V_{meso}

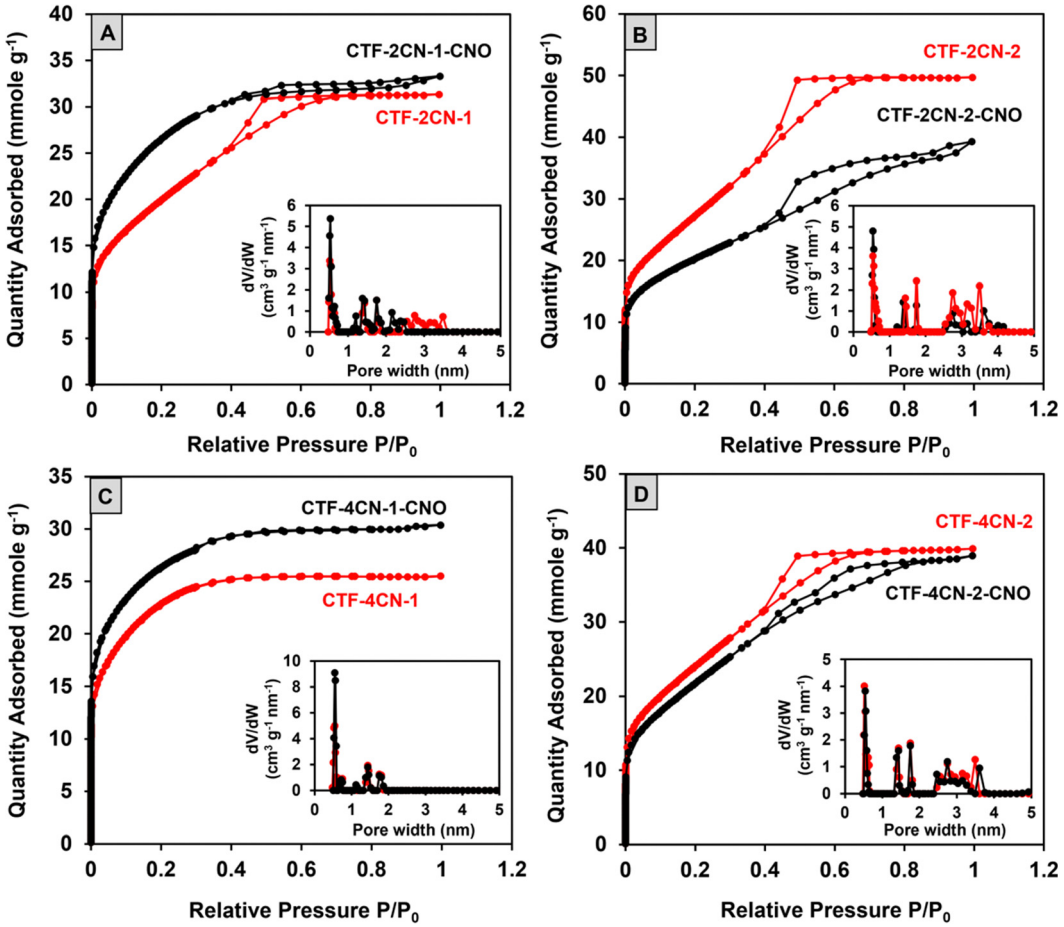

Fig. 6 N_2 adsorption–desorption isotherms and differential pore size distributions (inset) of the analyzed materials: (A) **CTF-2CN-1** and **CTF-2CN-1-CNO**; (B) **CTF-2CN-2** and **CTF-2CN-2-CNO**; (C) **CTF-4CN-1** and **CTF-4CN-1-CNO**; and (D) **CTF-4CN-2** and **CTF-4CN-2-CNO**.

Table 1 Textural characteristics of nanopores determined from low-temperature adsorption–desorption of N_2

Material	S_{BET} (m^2 g^{-1})	V_{micro} (cm^3 g^{-1})	V_{meso} (cm^3 g^{-1})	V_{total} (cm^3 g^{-1})
CTF-2CN-1	1612	0.55	0.52	1.10
CTF-2CN-1-CNO	2143	0.88	0.22	1.10
CTF-2CN-2	2260	0.62	1.09	1.71
CTF-2CN-2-CNO	1625	0.53	0.82	1.35
CTF-4CN-1	1835	0.82	0	0.82
CTF-4CN-1-CNO	2126	0.96	0	0.96
CTF-4CN-2	1962	0.63	0.73	1.36
CTF-4CN-2-CNO	1786	0.55	0.78	1.33

value, indicating a transformation of mesopores into micropores (Table 1, Fig. 6A inset and Fig. S6, ESI†). For the remaining systems in which the decrease in the nanopore volume occurred after CNO addition; for example, in the **CTF-4CN-1-CNO** system, the result was mainly caused by the decline in the V_{micro} and V_{meso} values (Table 1, Fig. 6C inset and Fig. S6, ESI†).

The nanopore diameters of all the studied systems were very similar. Namely, three groups of small ultramicropores (width smaller than 0.7 nm) with diameters of approximately 0.5 nm, and supermicropores with diameters of 1.4 nm and 1.8 nm were observed. Except for two microporous systems, the mesopore diameters were about 2.75 nm and 3.5 nm. The only exception was **CTF-2CN-2-CNO**, where mesopores of approximately 3.5 nm were not observed in the structure.

The cyclic voltammetry (CV) curves of all the synthesized **CTF** and **CTF–CNO** materials (Fig. 7A–D) indicated the capacitive nature of these materials, which is promising in the context of their potential use in SCs. On the other hand, the observed deviations from the shape of a perfect rectangle suggest the poor electrical conductivity of the tested material and the pseudocapacitance contribution in the electrode processes.

The last one is most likely due to the presence of N atoms in the skeleton of the synthesized CTF. Specifically, the CV

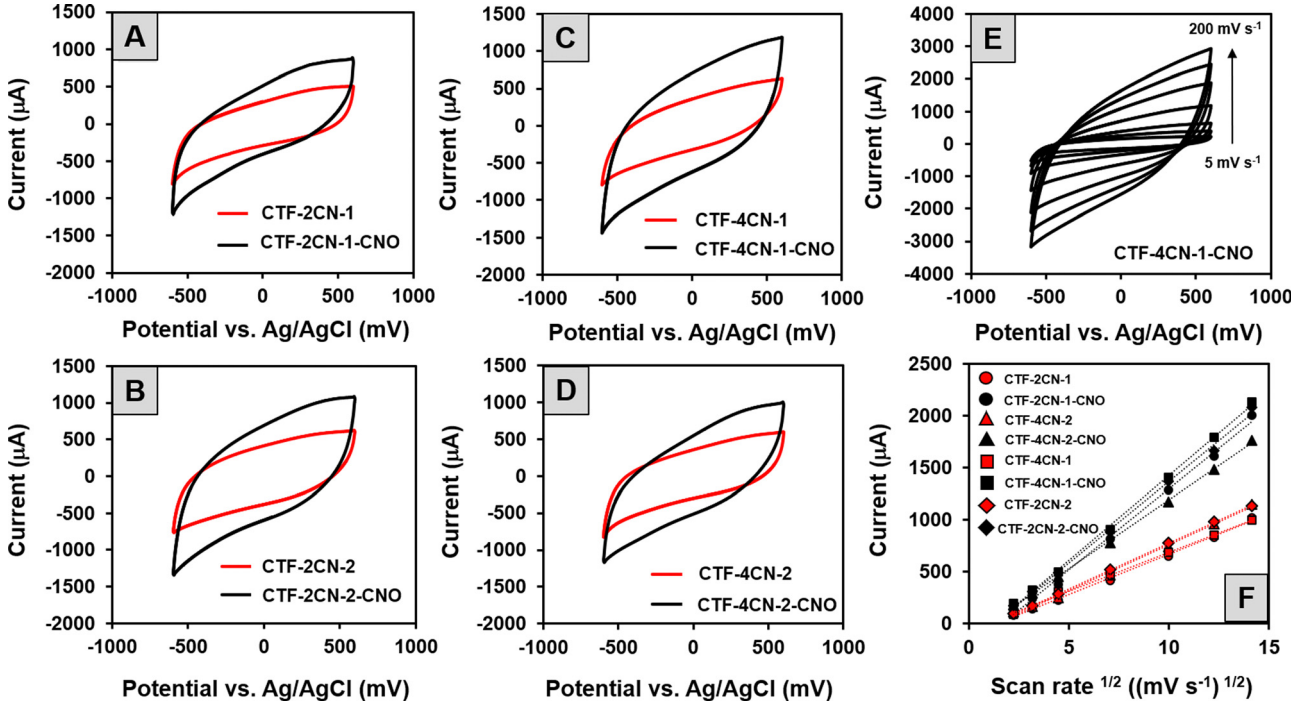

Fig. 7 (A)–(D) CVs of the GCE modified with different **CTF** and **CTF–CNO** materials recorded in a 1 M H_2SO_4 solution at a scan rate of 50 mV s^{-1}. (E) CVs of the GCE modified with **CTF-4CN-1-CNO** materials recorded at different scan rates (from 5 to 200 mV s^{-1}). (F) Dependence of current on the square root of the scan rate at 0.2 V.

Table 2 Specific capacitances, energy densities and power densities calculated from the CV and GCD studies

Material	C_S calculated from CV (F g^{-1})	C_S calculated from GCD (F g^{-1})	E_S (W h kg^{-1})	P_S (W kg^{-1})
CTF-2CN-1	204 ± 10	81 ± 5 (8 A g^{-1})	2	1712
CTF-2CN-1-CNO	366 ± 10	137 ± 8 (8 A g^{-1})	6	1996
CTF-2CN-2	294 ± 15	133 ± 5 (8 A g^{-1})	5	1842
CTF-2CN-2-CNO	486 ± 12	205 ± 10 (8 A g^{-1})	8	2007
CTF-4CN-1	250 ± 12	114 ± 10 (8 A g^{-1})	3	1674
CTF-4CN-1-CNO	495 ± 15	303 ± 6 (2 A g^{-1})	13	522
		278 ± 12 (4 A g^{-1})	12	1033
		258 ± 12 (6 A g^{-1})	10	1500
		237 ± 11 (8 A g^{-1})	9	1970
CTF-4CN-2	255 ± 10	123 ± 10 (8 A g^{-1})	4	1771
CTF-4CN-2-CNO	393 ± 10	171 ± 5 (8 A g^{-1})	6	1933

recorded for the **CTF** and **CTF–CNO** in 1 M H_2SO_4 solution exhibited deviations from a rectangular shape due to the protonation/deprotonation of N atoms with electron lone pairs exposed to an acidic solution.[79] It should also be emphasized that the addition of CNOs caused a significant increase in the electrochemical capacitance values of the composites compared to those of the corresponding pristine CTFs. The highest specific capacitances (C_s) calculated from CV measurements are summarized in Table 2, with values of 366 F g^{-1} (**CTF-2CN-1-CNO**), 393 F g^{-1} (**CTF-4CN-2-CNO**), 486 F g^{-1} (**CTF-2CN-2-CNO**) and 495 F g^{-1} (**CTF-4CN-1-CNO**). The influence of the scan rate on the current value, as recorded on the electrodes modified with the obtained materials, was also investigated. The CV recorded for the selected **CTF-4CN-1-CNO** material is shown in Fig. 7E. The analysis showed a linear relationship between the current recorded at 0.2 V *vs.* Ag/AgCl and the square root of the scan rate (Fig. 7F), which proves that the observed process was diffusion-controlled.

Further investigation of the mechanism of the electrode process was performed using electrochemical impedance spectroscopy (EIS). The Nyquist plots obtained for **CTF** and **CTF–CNO** materials differed in the spectrum range (Fig. S9, ESI†). The loop corresponding to the contact resistance between the electrode and the porous modifier layer, observed at high frequencies, was more significant in the EIS spectra recorded for pristine CTFs (Fig. S9A, ESI†). In turn, at low frequencies, the behavior of electrodes modified with **CTF–CNO** materials was strongly controlled by diffusion. It is evidenced by

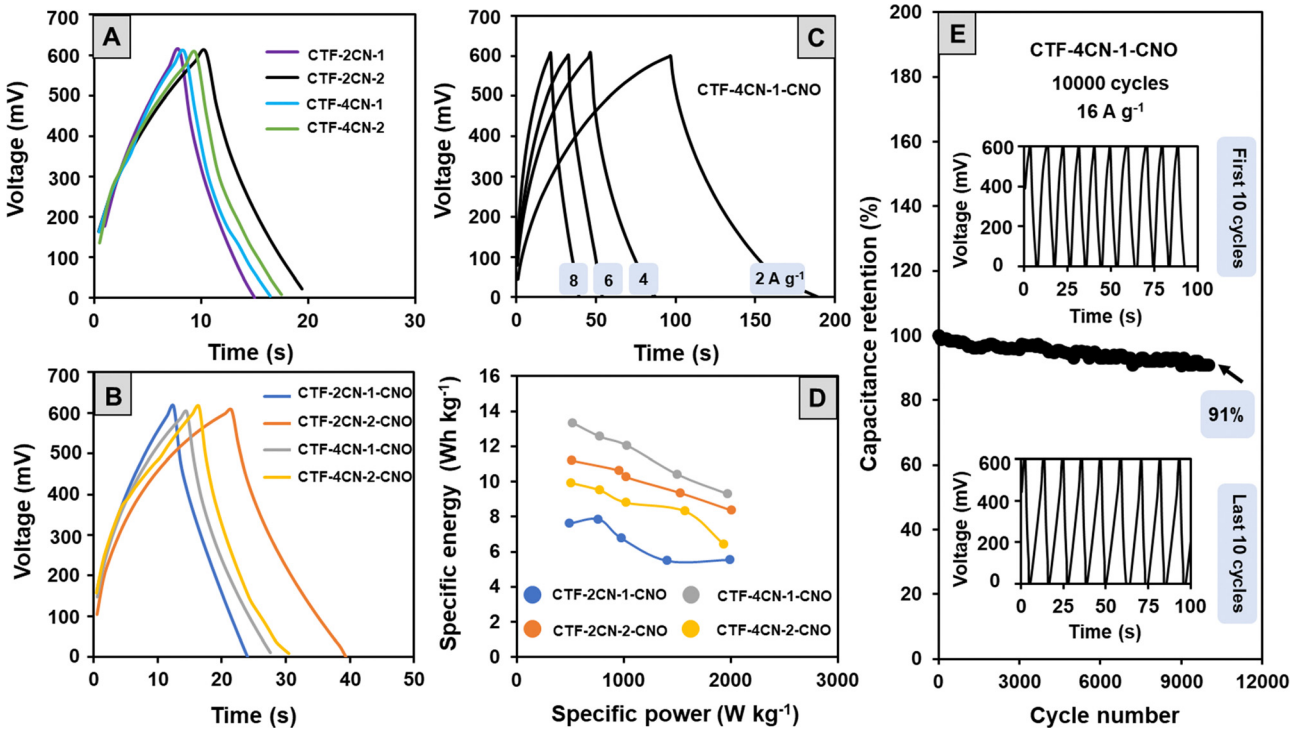

Fig. 8 (A) and (B) GCD curves of different materials recorded in 1 M H_2SO_4 at a specific current of 8 A g^{-1}. (C) GCD curves of **CTF-4CN-1-CNO** materials at different specific currents. (D) Ragone plots of the specific energy and power of **CTF–CNO** materials. (E) Capacitance retention as a function of cycle number for **CTF-4CN-1-CNO** materials at a specific current of 16 A g^{-1} (inset: first and last 10 GCD cycles).

the slope of the linear part of the Nyquist plot close to 45 degrees (Fig. S9B, ESI†). The impedance spectra of **CTF-4CN-1-CNO** recorded at different potentials (Fig. S9C, ESI†) confirm that this material can be used in the potential window from −0.6 to +0.6 V. The electrical equivalent circuit proposed for the obtained electrodes consists of a constant phase element (CPE) representing the capacitance, solution resistance (R_S), charge-transfer resistance (R_{ct}), and the Warburg impedance (Z_W) representing the transport of counter-ions through the layer during its charging (Fig. S9C inset, ESI†).

To confirm the electrochemical properties of the materials, they were also subjected to galvanostatic charge–discharge (GCD) tests with two-electrode configurations (Fig. 8A and B). In a wide positive potential window (0 to +0.6 V *vs.* Ag/AgCl), the GCD cycles showed a triangular shape with a slight deviation from a perfect profile observed in the part of the curve corresponding to the discharge process. The conclusions drawn from the GCD tests are similar to those obtained by the CV analysis. Namely, the studied materials showed a capacitive nature, but the course of the charging and discharging processes also indicated the participation of some pseudocapacitive currents.

The C_S values determined from the GCD measurements at a current density of 8 A g^{-1} were lower than the C_S values calculated from the CV curves (Table 2). This discrepancy results from relatively high current density and using a two-electrode configuration in the GCD electrochemical studies (CV measurements were carried out using a three-electrode system). The C_S values were also calculated for **CTF-4CN-1-CNO** at different current densities (Fig. 8C). The C_S value was 303 F g^{-1} at 2 A g^{-1}, 66% of this value (237 F g^{-1}). It indicates that the interconnected micropore structure provides an efficient pathway for the electrolyte ion movement through the porous carbon materials.

Analysis of the GCD cycles recorded for the **CTF–CNO** materials at different current densities, an example of which is shown in Fig. 8C, also allowed us to determine the values of energy density ($E_{density}$) and power density ($P_{density}$) (Table 2). The high active surface area of the porous electrodes increased $E_{density}$, while the charge storage mechanism of EDL led to a high $P_{density}$.[79] The relationship between these parameters is presented in Ragone plots (Fig. 8D). High values of $E_{density}$ indicate the excellent prospects of using the obtained structures to form SCs. For the material showing the best electrochemical properties (**CTF-4CN-1-CNO**), we also tested the capacitive retention after 10 000 cycles at a current density of 16 A g^{-1} (Fig. 8E). The capacitive retention was maintained at 91% of its initial value (Fig. 8E), and the shape of the recorded curves remained unchanged.

The C_S values calculated for the obtained materials in an aqueous acidic solution were much higher than those typically reported for carbon-based SCs (50–200 F g^{-1}).[80] In theESI,† we also showed a summary of the specific capacitance for other triazine systems in correlation with the materials obtained by our group (Table S6, ESI†). The C_S values of **CTF** and composite materials (CNO–CTF) are in the upper limit of the specific capacitance value, and a value of 303 (2 A g^{-1}) recorded in the

two-electrode system for **CTF-4CN-1-CNO** is the highest value recorded in the literature. The C_S values usually correlate with the specific surface area ranging from approximately 500 $m^2\ g^{-1}$ to 1000–2000 $m^2\ g^{-1}$. For our materials, with S_{BET} values ranging from 1800 to 2200 $m^2\ g^{-1}$, we achieved higher C_S values within the 200–500 F g^{-1} range for a three-electrode system and up to 300 F g^{-1} for a two-electrode system. The highest C_S value was obtained for the **CTF-4CN-1-CNO** material, for which S_{BET} was 2126 $m^2\ g^{-1}$, indicating the substantial contribution of microporosity.

3. Experimental

3.1. Materials

4-Cyanobenzaldehyde (98%), 4-cyanoaniline (98%), 2-amino-6-methylbenzothiazole (98%), 1,4-dicyanobenzene (98%), 7,7,8,8-tetracyanoquinodimethane (98%), iron(III) perchlorate hydrate $Fe(ClO_4)_3{\cdot}H_2O$ (crystalline), diacetyl (pure), and anhydrous zinc chloride (98%) were purchased from Sigma-Aldrich, USA. Glacial acetic acid (99.5–99.9%), methanol (99.8%), THF (99.5%), ethanol (96%), and concentrated hydrochloric acid (HCl) were purchased from Avantor Performance Materials Poland S.A. Toluene (99.8%), acetonitrile (99.8%), and dichlorobenzene (99%) were purchased from Sigma-Aldrich, USA. All reagents and solvents were used as received. Nanodiamond (ND, powder, 97 wt%, Carbodeon Diamond®Molto) with a crystal size of 4.2 ± 0.5 nm was used for the preparation of CNOs (annealing treatment under an inert atmosphere and reduced pressure of ultradispersed ND particles).[81]

The CTFs were labeled according to the number of nitrile groups (-CN). The CTFs with two –CN groups were denoted as **2CN-X** (1,4-dicyanobenzene and 1,4-bis(6-methylbenzo[*d*]-thiazol-2-yl)-2,5-bis(4-cyanophenyl)-1,4-dihydropyrrolo[3,2-*b*]pyrrole), and those with four –CN groups were denoted as **4CN-X** (7,7,8,8-tetracyanoquinodimethane and 1,2,4,5-tetrakis(4-cyanophenyl)-1,4-dihydropyrrolo[3,2-*b*]pyrrole), where *X* is 1 for known materials and 2 for new materials (pyrrolopyrrole-based).

All CTFs were synthesized by grinding the monomer with $ZnCl_2$ under inert conditions and placing the mixture in a quartz test tube. A significant excess of $ZnCl_2$ (5 weight, 5–23 molar equivalents, depending on the monomer's molar mass) was necessary to achieve complete dissolution. A Carbolite Gero STF 16/180 tube furnace was used for performing pyrolysis (with 3216 Controller).

3.2. Synthetic procedures

3.2.1. Synthesis of *N*-(4-cyanophenyl)aziridine-CNO (CNO-CN). CNOs (60 mg) were dispersed in dichlorobenzene (50 mL) by ultrasonication for 30 min. Then, 4-azidobenzonitrile (240 mg) in dichlorobenzene (10 mL) was added, and the mixture was heated at 120 °C for 12 h.[34] The reaction mixture was then ultrasonicated for 1 h and centrifuged for 10 min. The black powder collected at the bottom of the tube was washed three times with toluene and three times with methanol and then dried overnight in an oven (120 °C) to produce modified CNOs (70 mg).

3.2.2. General procedure A for the synthesis of tetrasubstituted 1,4-dihydropyrrolo[3,2-*b*]pyrroles. 4-Cyanobenzaldehyde (1048 mg, 8 mmol) and the appropriate aromatic amine (8 mmol) were added to a mixture of glacial acetic acid (8 mL) and toluene (8 mL). The mixture was stirred at 50 °C for 1 h. Then, $Fe(ClO_4)_3{\cdot}H_2O$ (6 mol%, 170 mg, 0.48 mmol) was added, followed by diacetyl (344 mg, 4 mmol). The resulting mixture was stirred at 50 °C in an open flask under an air atmosphere for 12 h.

2CN-2. *1,4-bis(6-methylbenzo[d]thiazole-2-yl)-2,5-bis(4-cyanophenyl)-1,4-dihydropyrrolo[3,2-b]pyrrole.* General procedure A was followed with 2-amino-6-methylbenzothiazole (1312 mg, 8 mmol). After the reaction, the solvents were evaporated, and the product was purified by crystallization from acetonitrile. After drying under vacuum, a yellow solid was obtained with a yield of 22% (1053 mg). ^{1}H NMR (500 MHz, $CDCl_3$) δ: 9.27 (s, 2H), 8.25 (d, J = 8.3 Hz, 4H), 8.05 (d, J = 8.3 Hz, 4H), 7.87 (m, 4H), 7.37 (d, J = 8.3 Hz, 2H), 2.46 (s, 6H) ppm; ^{13}C NMR (126 MHz, $CDCl_3$) δ = 170.0, 166.0, 149.8, 138.8, 136.0, 134.9, 133.5, 130.8, 128.8, 123.0, 122.5, 118.8, 115.3, 21.6 ppm; HRMS (TOF AP+): m/z calcd for $C_{36}H_{23}N_6S_2$: 603.1426 $[M + H]^+$; found: 603.1434.

4CN-2. *1,2,4,5-tetrakis(4-cyanophenyl)-1,4-dihydropyrrolo[3,2-b]pyrrole.* General procedure A was followed with 4-cyanoaniline (944 mg, 8 mmol). After the reaction, the precipitate was filtered off and washed with water and acetonitrile. The product was purified by crystallization from acetonitrile. After drying under vacuum, a yellow solid was obtained with a yield of 39% (792 mg). The ^{1}H NMR and ^{13}C NMR spectra were consistent with those previously reported.[37] HRMS (ESI^+): m/z calcd for $C_{34}H_{18}N_6$: 501.1593 $[M]^+$; found: 501.1596.

3.2.3. General procedure B for the synthesis of CTFs. The ground mixture of a substrate (200 mg) and dry $ZnCl_2$ (5–23 eq.) was placed in a quartz test tube under inert conditions, which was flame-sealed under vacuum and slowly heated to the desired temperature (700 °C) in a tube furnace (a heating rate of 1 °C per minute and then 48 h at the desired temperature). After cooling, the tube was opened, and the black monolithic material was ground thoroughly, washed with diluted HCl for 24 h several times with water and THF, and then dried at 120 °C overnight.

CTF-2CN-1. General procedure B was followed with dicyanobenzene (**2CN-1**, 200 mg, 1.56 mmol) and $ZnCl_2$ (1062 mg, 7.81 mmol, 5 eq.) to afford 154 mg of the product (77% yield) after purification and drying.

CTF-4CN-1. General procedure B was followed with 7,7,8,8-tetracyanoquinodimethane (**4CN-1**, 200 mg, 0.98 mmol) and $ZnCl_2$ (1067 mg, 7.84 mmol, 8 eq.) to afford 196 mg of the product (98% yield) after purification and drying.

CTF-2CN-2. General procedure B was followed with 1,4-bis(6-methylbenzo[*d*]thiazole-2-yl)-2,5-bis(4-cyanophenyl)-1,4-dihydropyrrolo[3,2-*b*]pyrrole (**2CN-2**, 200 mg, 0.33 mmol) and $ZnCl_2$

(1032 mg, 7.59 mmol, 23 eq.) to afford 182 mg of the product (91% yield) after purification and drying.

CTF-4CN-2. General procedure B was followed with 1,2,4,5-tetrakis(4-cyanophenyl)-1,4-dihydropyrrolo[3,2-*b*]pyrrole (**4CN-2**, 200 mg, 0.39 mmol) and $ZnCl_2$ (1066 mg, 7.84 mmol, 20 eq.) to afford 190 mg of the product (95% yield) after purification and drying.

3.2.4. General procedure C for the synthesis of CTF–CNO. The ground mixture of a substrate (100 mg), modified CNOs (**CNO-CN**, 5 mg), and dry $ZnCl_2$ (5–23 eq.) was placed in a quartz test tube under inert conditions, and the tube was flame-sealed under vacuum and slowly heated to the desired temperature (700 °C) in a tube furnace (a heating rate of 1 °C per minute and then 48 h at the desired temperature). After cooling, the tube was opened, and the black monolithic material was ground thoroughly and subsequently washed with diluted HCl for 24 h several times with water and THF and then dried at 120 °C overnight.

CTF-2CN-1-CNO. General procedure C was followed with dicyanobenzene (**2CN-1**, 100 mg, 0.78 mmol), **CNO-CN** (5 mg), and $ZnCl_2$ (531 mg, 3.91 mmol, 5 eq.) to afford 72 mg of the product (69% yield) after purification and drying.

CTF-4CN-1-CNO. General procedure C was followed with 7,7,8,8-tetracyanoquinodimethane (**4CN-1**, 100 mg, 0.49 mmol), **CNO-CN** (5 mg), and $ZnCl_2$ (533 mg, 3.92 mmol, 8 eq.) to afford 100 mg of the product (95% yield) after purification and drying.

CTF-2CN-2-CNO. General procedure C was followed with 1,4-bis(6-methylbenzo[*d*]thiazole-2-yl)-2,5-bis(4-cyanophenyl)-1,4-dihydropyrrolo[3,2-*b*]pyrrole (**2CN-2**, 100 mg, 0.17 mmol), **CNO-CN** (5 mg), and $ZnCl_2$ (520 mg, 3.82 mmol, 23 eq.) to afford 90 mg of the product (86% yield) after purification and drying.

CTF-4CN-2-CNO. General procedure C was followed with 1,2,4,5-tetrakis(4-cyanophenyl)-1,4-dihydropyrrolo[3,2-*b*]pyrrole (**4CN-2**, 100 mg, 0.2 mmol), **CNO-CN** (5 mg) and $ZnCl_2$ (533 mg, 3.92 mmol, 20 eq.) to afford 95 mg of the product (90% yield) after purification and drying.

4. Conclusions

In conclusion, we successfully synthesized pristine CTFs using 1,4-bis(6-methylbenzo[*d*]thiazol-2-yl)-2,5-bis(4-cyanophenyl)-1,4-dihydropyrrolo[3,2-*b*]pyrrole (**2CN-2**) and 1,2,4,5-tetrakis(4-cyanophenyl)-1,4-dihydropyrrolo[3,2-*b*]pyrrole (**4CN-2**) forming macrostructures with a repeating structural organization. This synthesized **CTF** was organized in a 3D manner on the CNO surface, creating **CTF–CNO** systems with the organized hierarchical porosity. This was achieved by adding only 5% by the weight of the CNO. A high porosity, about 2000 $m^2\ g^{-1}$, and interconnections between micropores and mesopores significantly increased the electrochemical performance of the obtained composites. The C_S value was increased 1.5–2 times compared to the reference **CTF** value, reaching 495 F g^{-1} in the three-electrode system in 1 M H_2SO_4 (**CTF-4CN-1-CNO**). Using the GCD method in a two-electrode system, the C_S value of the same system was 303 (2 A g^{-1}), reaching the highest value from the literature data for triazine systems. For the material showing the best electrochemical properties (**CTF-4CN-1-CNO**), we also tested the capacitive retention at a current density of 16 A g^{-1} that was at 91% of the initial value after 10 000 cycles, and the shape of the recorded curves remained unchanged.

Apart from high porosity, several factors may be responsible for such a significant increase in electrochemical performance. The presence of highly graphitized domains characterized the **CNO–CTF** materials we obtained, the interconnected pores preventing the walls of the pores from pulverizing while exhibiting an extremely high level of structural integrity, morphological heterogeneity resulting from the simultaneous presence of amorphous phases and crystalline zones that may result in higher structural stability and higher conductivity of the hybrid materials, a high percentage of the pyridinic-N, pyrrolic-N and graphitic-N atoms, which are responsible for the pseudocapacitance in materials. The efficient combination of all these factors made composites excellent electrode materials. Due to these features, the **CTF–CNO** materials showed attractive properties for practical applications in electrochemistry.

Author contributions

Conceptualization, methodology, supervision, project administration, visualization, data curation and funding acquisition: M. E. P.-B. methodology, visualization, validation, formal analysis and investigation: A. H., G. S., J. B., K. B., A. I. and A. P. T. The manuscript was written through contributions of all authors. All authors have given approval to the final version of the manuscript.

Conflicts of interest

There are no conflicts to declare.

Note added after first publication

This article replaces the version published on 4th December 2023, which contained errors in Fig. 7 and 8.

Acknowledgements

We gratefully acknowledge the financial support from the National Science Centre, Poland, grants #2017/25/B/ST5/01414 and #2019/35/B/ST5/00572 to M. E. P.-B. We gratefully acknowledge Prof. Luis Echegoyen from the University of Texas at El Paso for providing the CNOs. The research was carried out with the equipment purchased thanks to the financial support of the European Regional Development Fund (POIG.02.01.00-06024/09, Maria Curie-Sklodowska University, Poland).

References

1 M. E. Plonska-Brzezinska and L. Echegoyen, *J. Mater. Chem. A*, 2013, **1**, 13703.
2 R. Kumar, E. Joanni, S. Sahoo, J.-J. Shim, W. K. Tan, A. Matsuda and R. K. Singh, *Carbon*, 2022, **193**, 298–338.
3 Y. Soneda, *Handbook of Advanced Ceramics*, Elsevier, 2013, pp. 211–222.
4 H. Aghajani, A. T. Tabrizi, R. Ghorbani, S. Behrangi, M. Stupavska and N. Abdian, *J. Alloys Compd.*, 2022, **906**, 164284.
5 A. Hryniewicka, J. Breczko, G. Siemiaszko, A. N. Papathanassiou, K. Góra-Marek, K. A. Tarach, K. Brzezinski, A. Ilnicka, A. P. Terzyk, K. H. Markiewicz, L. Echegoyen and M. E. Plonska-Brzezinska, *Sci. Rep.*, 2023, **13**, 10737.
6 A. Hryniewicka, J. Breczko, G. Siemiaszko, K. Brzezinski, A. Ilnicka, A. Terzyk and M. Plonska-Brzezinska, *ChemRXiv*, 2022, preprint, DOI: 10.26434/chemrxiv-2022-qpgjj.
7 M. Zhong, M. Zhang and X. Li, *Carbon Energy*, 2022, **4**, 950–985.
8 G. Siemiaszko, J. Breczko, A. Hryniewicka, A. Ilnicka, K. H. Markiewicz, A. P. Terzyk and M. E. Plonska-Brzezinska, *Sci. Rep.*, 2023, **13**, 6606.
9 G. Siemiaszko, A. Hryniewicka, J. Breczko, O. F. Delgado, K. H. Markiewicz, L. Echegoyen and M. E. Plonska-Brzezinska, *ACS Appl. Polym. Mater.*, 2022, **4**, 2442–2458.
10 G. Siemiaszko, A. Hryniewicka, J. Breczko, K. Brzezinski and M. E. Plonska-Brzezinska, *Chem. Commun.*, 2022, **58**, 6829–6832.
11 M. E. Plonska-Brzezinska, *ChemNanoMat*, 2019, **5**, 568–580.
12 L. Zhou, C. Gao, D. Zhu, W. Xu, F. F. Chen, A. Palkar, L. Echegoyen and E. S.-W. Kong, *Chem. – Eur. J.*, 2009, **15**, 1389–1396.
13 O. Mykhailiv, M. Imierska, M. Petelczyc, L. Echegoyen and M. E. Plonska-Brzezinska, *Chem. – Eur. J.*, 2015, **21**, 5783–5793.
14 S. Sek, J. Breczko, M. E. Plonska-Brzezinska, A. Z. Wilczewska and L. Echegoyen, *ChemPhysChem*, 2013, **14**, 96–100.
15 M. Bartkowski and S. Giordani, *Nanoscale*, 2020, **12**, 9352–9358.
16 M. E. Plonska-Brzezinska, A. Molina-Ontoria and L. Echegoyen, *Carbon*, 2014, **67**, 304–317.
17 J. K. McDonough, A. I. Frolov, V. Presser, J. Niu, C. H. Miller, T. Ubieto, M. V. Fedorov and Y. Gogotsi, *Carbon*, 2012, **50**, 3298–3309.
18 F.-D. Han, B. Yao and Y.-J. Bai, *J. Phys. Chem. C*, 2011, **115**, 8923–8927.
19 N. Keller, N. I. Maksimova, V. V. Roddatis, M. Schur, G. Mestl, Y. V. Butenko, V. L. Kuznetsov and R. Schlögl, *Angew. Chem., Int. Ed.*, 2002, **41**, 1885–1888.
20 C. Portet, G. Yushin and Y. Gogotsi, *Carbon*, 2007, **45**, 2511–2518.
21 C. Zhu, F. Xu, J. Chen, H. Min, H. Dong, L. Tong, K. Qasim, S. Li and L. Sun, *J. Power Sources*, 2016, **303**, 159–167.
22 Y. Zhang and S. Jin, *Polymers*, 2019, **11**, 31.
23 L. Hao, B. Luo, X. Li, M. Jin, Y. Fang, Z. Tang, Y. Jia, M. Liang, A. Thomas, J. Yang and L. Zhi, *Energy Environ. Sci.*, 2012, **5**, 9747–9751.
24 L. Hao, J. Ning, B. Luo, B. Wang, Y. Zhang, Z. Tang, J. Yang, A. Thomas and L. Zhi, *J. Am. Chem. Soc.*, 2015, **137**, 219–225.
25 Y. Su, Y. Liu, P. Liu, D. Wu, X. Zhuang, F. Zhang and X. Feng, *Angew. Chem., Int. Ed.*, 2015, **54**, 1812–1816.
26 M. G. Mohamed, S. U. Sharma, N.-Y. Liu, T. H. Mansoure, M. M. Samy, S. V. Chaganti, Y.-L. Chang, J.-T. Lee and S.-W. Kuo, *Int. J. Mol. Sci.*, 2022, **23**, 3174.
27 M. G. Mohamed, A. F. M. EL-Mahdy, M. M. M. Ahmed and S. Kuo, *ChemPlusChem*, 2019, **84**, 1767–1774.
28 M. G. Mohamed, A. F. M. EL-Mahdy, Y. Takashi and S.-W. Kuo, *New J. Chem.*, 2020, **44**, 8241–8253.
29 M. M. Vadiyar, X. Liu and Z. Ye, *ACS Appl. Mater. Interfaces*, 2019, **11**, 45805–45817.
30 Y. Li, S. Zheng, X. Liu, P. Li, L. Sun, R. Yang, S. Wang, Z.-S. Wu, X. Bao and W.-Q. Deng, *Angew. Chem., Int. Ed.*, 2018, **57**, 7992–7996.
31 Y. Zhang, B. Zhang, L. Chen, T. Wang, M. Di, F. Jiang, X. Xu and S. Qiao, *J. Colloid Interface Sci.*, 2022, **606**, 1534–1542.
32 Y. Gao, C. Zhi, P. Cui, K. A. I. Zhang, L.-P. Lv and Y. Wang, *Chem. Eng. J.*, 2020, **400**, 125967.
33 C. Wu, H. Zhang, M. Hu, G. Shan, J. Gao, J. Liu, X. Zhou and J. Yang, *Adv. Electron. Mater.*, 2020, **6**, 2000253.
34 A. Hryniewicka, J. Breczko, G. Siemiaszko, A. Papathanassiou, K. Góra-Marek, K. A. Tarach, K. Brzezinski, A. Ilnicka, A. P. Terzyk, K. H. Markiewicz, L. Echegoyen and M. E. Plonska-Brzezinska, *ChemRXiv*, 2022, preprint, DOI: 10.26434/chemrxiv-2022-h0n3l.
35 P. Kuhn, M. Antonietti and A. Thomas, *Angew. Chem., Int. Ed.*, 2008, **47**, 3450–3453.
36 D. H. Friese, A. Mikhaylov, M. Krzeszewski, Y. M. Poronik, A. Rebane, K. Ruud and D. T. Gryko, *Chem. – Eur. J.*, 2015, **21**, 18364–18374.
37 M. Tasior, O. Vakuliuk, D. Koga, B. Koszarna, K. Górski, M. Grzybowski, L. Kielesinski, M. Krzeszewski and D. T. Gryko, *J. Org. Chem.*, 2020, **85**, 13529–13543.
38 N. A. Elessawy, J. El Nady, W. Wazeer and A. B. Kashyout, *Sci. Rep.*, 2019, **9**, 1129.
39 C. Xia, X. Hai, X.-W. Chen and J.-H. Wang, *Talanta*, 2017, **168**, 269–278.
40 N. A. Kumar, H. Nolan, N. McEvoy, E. Rezvani, R. L. Doyle, M. E. G. Lyons and G. S. Duesberg, *J. Mater. Chem. A*, 2013, **1**, 4431–4435.
41 A. Kellenberger, E. Dmitrieva and L. Dunsch, *Phys. Chem. Chem. Phys.*, 2011, **13**, 3411.
42 C. M. Masemola, N. Moloto, Z. N. Tetana, S. S. Gqoba, P. K. Mubiayi and E. C. Linganiso, *Mater. Chem. Phys.*, 2022, **287**, 126229.
43 K. Wang, L.-M. Yang, X. Wang, L. Guo, G. Cheng, C. Zhang, S. Jin, B. Tan and A. Cooper, *Angew. Chem., Int. Ed.*, 2017, **56**, 14149–14153.
44 S. Mukherjee, M. Das, A. Manna, R. Krishna and S. Das, *J. Mater. Chem. A*, 2019, **7**, 1055–1068.
45 M. Koinuma, H. Tateishi, K. Hatakeyama, S. Miyamoto, C. Ogata, A. Funatsu, T. Taniguchi and Y. Matsumoto, *Chem. Lett.*, 2013, **42**, 924–926.
46 M. K. Rabchinskii, S. A. Ryzhkov, D. A. Kirilenko, N. V. Ulin, M. V. Baidakova, V. V. Shnitov, S. I. Pavlov, R. G. Chumakov, D. Y. Stolyarova, N. A. Besedina, A. V. Shvidchenko, D. V. Potorochin, F. Roth, D. A. Smirnov, M. V. Gudkov,

M. Brzhezinskaya, O. I. Lebedev, V. P. Melnikov and P. N. Brunkov, *Sci. Rep.*, 2020, **10**, 6902.
47 Y.-C. Chiang, Y.-J. Chen and C.-Y. Wu, *Materials*, 2017, **10**, 1296.
48 A. Barinov, O. B. Malcioglu, S. Fabris, T. Sun, L. Gregoratti, M. Dalmiglio and M. Kiskinova, *J. Phys. Chem. C*, 2009, **113**, 9009–9013.
49 D. Y. Osadchii, A. I. Olivos-Suarez, A. V. Bavykina and J. Gascon, *Langmuir*, 2017, **33**, 14278–14285.
50 T. Wei, Q. Zhang, X. Wei, Y. Gao and H. Li, *Sci. Rep.*, 2016, **6**, 22646.
51 N. K. Gupta, B. Peng, G. L. Haller, E. E. Ember and J. A. Lercher, *ACS Catal.*, 2016, **6**, 5843–5855.
52 R. Arrigo, M. Hävecker, S. Wrabetz, R. Blume, M. Lerch, J. McGregor, E. P. J. Parrott, J. A. Zeitler, L. F. Gladden, A. Knop-Gericke, R. Schlögl and D. S. Su, *J. Am. Chem. Soc.*, 2010, **132**, 9616–9630.
53 S. Chen, X. Hai, C. Xia, X.-W. Chen and J.-H. Wang, *Chem. – Eur. J.*, 2013, **19**, 15918–15923.
54 Y. Yang, Z. Lu, J. Xia, Y. Liu, K. Wang and X. Wang, *Chem. Eng. Sci.*, 2021, **229**, 116054.
55 Z. Liu, X. Yuan, S. Zhang, J. Wang, Q. Huang, N. Yu, Y. Zhu, L. Fu, F. Wang, Y. Chen and Y. Wu, *NPG Asia Mater.*, 2019, **11**, 12.
56 G. Lui, G. Li, X. Wang, G. Jiang, E. Lin, M. Fowler, A. Yu and Z. Chen, *Nano Energy*, 2016, **24**, 72–77.
57 D. McNulty, E. Carroll and C. O'Dwyer, *Adv. Energy Mater.*, 2017, **7**, 1602291.
58 L. J. Fu, T. Zhang, Q. Cao, H. P. Zhang and Y. P. Wu, *Electrochem. Commun.*, 2007, **9**, 2140–2144.
59 S. Tomita, M. Fujii and S. Hayashi, *Phys. Rev. B: Condens. Matter Mater. Phys.*, 2002, **66**, 245424.
60 S. Tomita, A. Burian, J. C. Dore, D. LeBolloch, M. Fujii and S. Hayashi, *Carbon*, 2002, **40**, 1469–1474.
61 A. E. Aleksenskii, M. V. Baidakova, A. Y. Vul', V. Y. Davydov and Y. A. Pevtsova, *Phys. Solid State*, 1997, **39**, 1007–1015.
62 Q.-H. Yang, P.-X. Hou, M. Unno, S. Yamauchi, R. Saito and T. Kyotani, *Nano Lett.*, 2005, **5**, 2465–2469.
63 S.-W. Bian, Z. Ma and W.-G. Song, *J. Phys. Chem. C*, 2009, **113**, 8668–8672.
64 A. Vinu, P. Srinivasu, D. P. Sawant, T. Mori, K. Ariga, J.-S. Chang, S.-H. Jhung, V. V. Balasubramanian and Y. K. Hwang, *Chem. Mater.*, 2007, **19**, 4367–4372.
65 T. Komatsu, *Macromol. Chem. Phys.*, 2001, **202**, 19–25.
66 B. V. Lotsch, M. Döblinger, J. Sehnert, L. Seyfarth, J. Senker, O. Oeckler and W. Schnick, *Chem. – Eur. J.*, 2007, **13**, 4969–4980.
67 A. Schwarzer, T. Saplinova and E. Kroke, *Coord. Chem. Rev.*, 2013, **257**, 2032–2062.
68 W. Ruland and B. Smarsly, *J. Appl. Crystallogr.*, 2002, **35**, 624–633.
69 F. Fina, S. K. Callear, G. M. Carins and J. T. S. Irvine, *Chem. Mater.*, 2015, **27**, 2612–2618.
70 D. M. Teter and R. J. Hemley, *Science*, 1996, **271**, 53–55.
71 X. Wang, K. Maeda, A. Thomas, K. Takanabe, G. Xin, J. M. Carlsson, K. Domen and M. Antonietti, *Nat. Mater.*, 2009, **8**, 76–80.
72 M. Kim, S. Hwang and J.-S. Yu, *J. Mater. Chem.*, 2007, **17**, 1656–1659.
73 J. Rouquerol, P. Llewellyn and F. Rouquerol, *Studies in Surface Science and Catalysis*, Elsevier, 2007, vol. 160, pp. 49–56.
74 C. Lastoskie, K. E. Gubbins and N. Quirke, *J. Phys. Chem.*, 1993, **97**, 4786–4796.
75 P. Tarazona, *Mol. Phys.*, 1984, **52**, 81–96.
76 J. P. Olivier, *J. Porous Mater.*, 1995, **2**, 9–17.
77 M. Thommes, K. Kaneko, A. V. Neimark, J. P. Olivier, F. Rodriguez-Reinoso, J. Rouquerol and K. S. W. Sing, *Pure Appl. Chem.*, 2015, **87**, 1051–1069.
78 B. Lobato, L. Suárez, L. Guardia and T. A. Centeno, *Carbon*, 2017, **122**, 434–445.
79 M. Zhong, E. K. Kim, J. P. McGann, S.-E. Chun, J. F. Whitacre, M. Jaroniec, K. Matyjaszewski and T. Kowalewski, *J. Am. Chem. Soc.*, 2012, **134**, 14846–14857.
80 C. Liu, F. Li, L.-P. Ma and H.-M. Cheng, *Adv. Mater.*, 2010, **22**, E28–E62.
81 V. L. Kuznetsov and Yu. V. Butenko, in *Synthesis, Properties and Applications of Ultrananocrystalline Diamond*, ed. D. M. Gruen, O. A. Shenderova and A. Y. Vul', Springer-Verlag, Berlin/Heidelberg, 2005, vol. 192, pp. 199–216.